Synthesis, Structural Characterization, Dielectric and Piezoelectric Properties of Multiferroic Double-perovskite Bi$_2$FeMnO$_6$ Ceramics

Peng Song, Zhipeng Pei, Heng Wu, Yao Lu, Weiren Xia, Xinhua Zhu*

National Laboratory of Solid State Microstructures, School of Physics, Nanjing University, Nanjing 210093, China

*Corresponding author: E-mail: xhzhu@nju.edu.cn

Abstract

Double-perovskite structured multiferroic Bi$_2$FeMnO$_6$ (BFMO) ceramics synthesized *via* solid-state reaction route at 880°C for 3 h, crystallized in a distorted rhombohedral structure with *R*3*c* space group. Their lattice parameters in the hexagonal system were determined to be a = 5.571 Å and c = 13.191 Å. SEM images show that the BFMO ceramic grains exhibit spherical morphology with an average size of 6.70 μm. Their atomic ratio of Bi:Fe:Mn was determined to be 2.07:1.02:1.00, close to the nominal value of 2:1:1. Raman spectra have verified the vibrational frequencies in the BFMO ceramics, and only 11 Raman active modes are observed. The less observed Raman modes in the BFMO ceramics compared with the theoretical group analyses, can be ascribed to the small correlation field splitting of the ceramic samples due to their polycrystalline nature. BFMO ceramics exhibit almost frequency-independent dielectric behavior in a frequency range of 500 - 10^6 Hz at room temperature. Their dielectric constant and dielectric loss were measured to be 700 and 0.03 at 10^6 Hz, respectively. The piezoelectric moduli d_{33} of the poled BFMO ceramics was measured to be 56 pC/N, which is two times larger than that reported for BiFeO$_3$ thin film (d_{33} ≅ 25 pC/N). Copyright © VBRI Press.

Keywords: Double perovskite oxides, Bi$_2$FeMnO$_6$ multiferroic ceramics, Raman spectra, dielectric and piezoelectric properties, microstructural characterization.

Introduction

In recent years, multiferroic materials where the ferroelectric and magnetic ordering coexist, have drawn considerable attention due to their fundamental physical characteristics and extensive applications in the fields of tunable multifunctional spintronics, magnetoelectric random access memory devices and photovoltaic cells [**1, 2**]. As the paradigm of magnetoelectric multiferroic materials at room temperature, BiFeO$_3$ (BFO) is the most systematically investigated in the past decade [**3, 4**]. However, as a canted antiferromagnet BFO exhibits a very weak ferromagnetism and its remnant magnetization is only about 1 ~ 10 emu/cm^3 [**5-7**]. Additionally, it has some inherent problems such as high leakage current, structural instability, and the formation of multiphase system during the synthesis process. These drawbacks of BFO limit its applications in multiferroic devices, therefore, much efforts to explore new candidate multiferroic materials are highly desirable. In terms of searching for new room-temperature magnetoelectric multiferroic materials, ordered double perovskites (Bi$_2$B′B″O$_6$, B′or B″ = transition metals such as Ni, Mn, Fe, and Co) with bismuth on the A site have gained much interests [**8-10**]. In these compounds, due to the large orbital radius of the Bi 6s^2 lone-pair electrons at A site, the crystal structure is usually distorted to low symmetries, inducing large ferroelectric polarization, while the B-site ordering of transition-metal ions (B′and B″) makes such material ferromagnetic or anti-ferromagnetic through the B′-O-B″-O-B′ super-exchanging interactions mediated by itinerant electrons [**11-13**]. Among these materials, B-site ordered Bi$_2$NiMnO$_6$ and Bi$_2$FeCrO$_6$ have been widely investigated [**14-22**], in contrast only a few studies are focused on the Bi$_2$FeMnO$_6$ (BFMO) due to the difficulties in the synthesis of pure phase BFMO *via* a conventional high temperature solid-state reactions [**23-25**]. Zhao *et al.* [**23, 24**] synthesized the BFMO ceramics *via* conventional solid-state reaction method by using Bi$_2$O$_3$, Fe$_3$O$_4$, and MnCO$_3$ as starting materials with 10 mol% extra Bi$_2$O$_3$. The impure phase of Bi$_2$Fe$_4$O$_9$ was detected in the BFMO ceramics, which usually appeared in the BiFeO$_3$ ceramics. To stabilize the metastable phase of BFMO, partial replacement of Bi by La (20 mol%) in BFMO was performed. They found the La-doped BFMO ceramics exhibited a spin glass state at low temperature with a T$_N$ below room temperature [**23**]. It is reported that the applications of external high pressure can

enhance the ability of the perovskite to accommodate different ionic sizes, vacancies, and the structural distortions derived from the mismatch of A-O and B-O bond distances, the Jahn-Teller distortions (elongation/compression) and buckling (variation of the B-O-B angle) of the BO_6 octahedra [26]. Delmonte *et al.* [25] prepared the metastable BFMO ceramics *via* a solid-state reaction under high pressure (6 GPa) and temperature (1100°C for 1.5 h). The as-prepared BFMO ceramics showed a distorted, centrosymmetric orthorhombic cell with *Pnam* space group (induced by Bi^{3+} stereochemical effect), in which a small amount (< 6 wt%) of bismuth oxycarbonate (Bi_2CO_5) was observed. That was formed by the reaction of Bi_2O_3 and carbon dioxide generated by the heating of the graphite furnace during the high pressure and high temperature reaction, such reaction should be considered as an unavoidable process. The as-prepared BFMO ceramics exhibited an antiferromagnetic behavior with a $T_N = 288$ K. In addition, a semiconductor-insulator phase transition was observed at $T_P \approx 140$ K. Different electrical properties were measured in the as-prepared BFMO ceramics within three distinct temperature ranges (e.g., $T > T_N$, $T_N > T > T_P$, and $T < T_P$). To make full use of the multiferroic properties of BFMO materials in the field of information storage devices, the ferroelectric and magnetic properties of BFMO thin films have received much attention [27-34]. For example, Zhao *et al.* [27] investigated the multiferroic properties of Nd:BFO/BFMO bilayer films deposited on Pt/Ti/SiO₂/Si substrate by pulsed laser deposition (PLD) method, and they found that the films underwent a ferromagnetic transition at 440 K and exhibited both ferrimagnetism and ferroelectricity at room temperature. Choi *et al.* [28] reported that the strained BFMO films grown on SrTiO₃ (001) substrates exhibited a strong enhancement of the magnetization and the magnetic transition temperature, indicating the importance of strain effect on the magnetism of BFMO. Significant differences observed in the magnetic moments between much thinner and thicker films can be ascribed to the fact that much thinner thin films are highly strained and tetragonal whereas the thick films are more relaxed and monoclinic. Theoretically, the first-principles calculations on the thick films demonstrate that the full relaxation of the atomic coordinates and lattice vectors in the thick films results in the most stable monoclinic structure without a magnetic ordering [8]. Ahmed *et al.* [29, 30] investigated the magnetization of BFMO films by X-ray magnetic circular dichroism measurements, and the electronic and optical properties of BFMO films by using density functional theory calculations. Du *et al.* [31] reported the magnetic properties of BFMO thin films deposited by electrospray method. Three magnetic transitions at 150 K, 260 K, and 440 K were observed in the BFMO thin films, respectively, which correspond to the ferromagnetic Fe-O-Mn, antiferromagnetic Mn-O-Mn and Fe-O-Fe orderings. Such magnetic transitions were also confirmed by heat capacity measurements. Liu *et al.*

[32] investigated the growth mechanisms, dielectricity and magnetism of multiferroic BFMO epitaxial thin films deposited by PLD on different Nb-doped SrTiO₃ substrates. It is found that the substrate orientations play an import role in controlling the crystal growth behaviors of the epitaxial BFMO thin films. Particularly, a spiral growth morphology was observed in the BFMO thin film deposited on (100) Nb-doped SrTiO₃ substrate, which is ascribed to the formation of screw dislocation defects during the deposited process. All the epitaxial BFMO thin films exhibit weak ferromagnetic behavior at 200 K, which is indicated by saturated hysteresis loops with very small coercive fields. Recently, Sun *et al.* [33] examined the microstructures of epitaxial BFMO thin films and confirmed the Fe-Mn alternative ordering in the [111] direction by both synchrotron X-ray reciprocal space mapping and high-resolution transmission electron microscopy. In spite of the epitaxial BFMO thin films exhibiting the interesting coexistence of ferroelectricity and spin-glass state, the large leakage currents of the BFMO thin films makes the polarization-electric field (P-E) hysteresis loops measured impossible at room temperature. Shen *at al.* [34] explored the leakage mechanisms of the BFMO epitaxial thin films, and found four different leakage mechanisms involved in BFMO thin films, which are dependent upon the electric field strength. As transition-metal oxides, oxygen vacancies intrinsically exist in the BFMO. The oxygen vacancy effect on double perovskite BFMO is recently investigated by first-principles simulations using density functional theory [35]. The evolution of magnetic moment and the change in electronic structure with the vacancy concentration are numerically demonstrated. A strong on-site Hubbard interactions is critical for the gap opening in a pristine BFMO. In the presence of 2.08% oxygen vacancy, BFMO become metallic and the average magnetization is decreased with increasing the oxygen vacancy concentration. An insulator-metal transition or crossover is identified with oxygen in BFMO based on the calculations of band structure and optical conductivity. Besides the BFMO thin films, double-perovskite BFMO nano-/micron-sized hollow particles are also synthesized [36], which exhibit a weak ferromagnetic-like behavior at both low and room temperature.

Despite these previous studies, up to date only a few works on the BFMO ceramics are reported due to the difficulties of synthesizing this metastable material through a conventional high temperature synthesis process. Therefore, reports on the detailed physical properties of this material are still awaited with great interest. In this work, we report on the synthesis of double-perovskite BFMO ceramics by conventional solid-state reaction method, and their microstructures were investigated by X-ray diffraction (XRD), scanning electron microscopy (SEM), and X-ray energy dispersive spectroscopy (EDS), and Raman spectra. Furthermore, the dielectric and piezoelectric properties of the double-perovskite BFMO ceramics are also reported.

Experimental procedure

In this work, double-perovskite BFMO ceramic samples were synthesized by solid-state reaction method, where the analytical reagent grade powders of Bi_2O_3, Fe_3O_4 and $MnCO_3$ (> 99.5% purity) (Sigma-Aldrich (Shanghai) Trading Co., Ltd.) were used as the starting materials. Before the synthesis of double-perovskite BFMO ceramic samples, we perform the differential scanning calorimetry (DSC) and thermal gravimetric (TG) analysis (DSC-TG) of the mixed oxide powders of Bi_2O_3, Fe_3O_4 and $MnCO_3$, to determine the suitable sintering temperature. The DSC-TG tests were performed on a Mettler-Toledo TGA/DSC2 thermal analyzer. The oxide powders of Bi_2O_3, Fe_3O_4 and $MnCO_3$ were weighed and mixed according to the molar ratios of Bi:Fe:Mn = 1.1:1.0:2.0. The 10 mol % excess Bi_2O_3 was added to the mixture to compensate for the loss of Bi_2O_3 during the sintering process. The mixture was pre-sintered at 800ºC for 3 h, and then ball-milled to fine powders, dried and pressed into pellets of 10 mm diameter under a pressure of 30 MPa. Disc samples were sintered in an alumina crucible at 880ºC for 3 h in air, and then cooled naturally to room temperature. The crystal structure of the ceramic samples was examined by powder XRD at room temperature (Rigaku D/max-RA) by using Cu-$K\alpha$ radiation at λ = 1.54056 Å. The microstructures of the ceramic samples were characterized by SEM (S-3400N II, Hitachi) equipped with an X-ray energy dispersive spectroscopy (EDS, EX-250 spectroscopy). Raman spectroscopy measurements with a shift range from 100 to 1200 cm^{-1} were performed with a laser Raman spectrometer (Model 2501 PC, Shimadzu) at room temperature, employing an Ar^+ laser with wavelength of 514 nm for excitation of the Raman signals.

For the dielectric measurements, the surfaces of the sintered BFMO pellets were polished followed by coating a silver paste on the both sides. The silver pastes were fired at 550ºC for 30 min. The dielectric properties of the sintered BFMO ceramics were measured at room temperature from 500 to 10^6 Hz using an HP 4192 A impedance analyzer. Before the piezoelectric measurement, the ceramic samples were first poled in the silicon oil at 120ºC for 30 minutes under an electric field of 30 kV/cm. After ageing for 24 h, the piezoelectric modulus d_{33} of the ceramic samples was measured with a standard d_{33} piezometer (Model ZJ-4AN, the Institute of Acoustics of the Chinese Academy of Science, China).

Results and discussion

Fig. 1 illustrates the DSC-TG curves of the mixed oxide powders of Bi_2O_3, Fe_3O_4 and $MnCO_3$. It is observed that on the TG curve, the first weight loss of 1.30% between room temperature and 300ºC (endothermic DSC peak at 200ºC), corresponds to the removal of water weakly adsorbed on the surface of the oxide powders. The second weight loss step, of ~ 4.87 % occurring between 300 and 600ºC (predominantly endothermic DSC peaks at around 330ºC and 540ºC), is assigned to the

decomposition process of $MnCO_3$ into MnO_2 [37]. In the temperature range from 600ºC to 800ºC there is a slight increase of weight (0.83%) on the TG curve, corresponding to the transfer from MnO_2 to Mn_2O_3 [37]. In the temperature region from 800ºC to 900ºC there is no apparent change in the weight, indicating the crystallization process of the mixture. However, an obvious endothermic peak at around 890ºC is observed on the DSC curve, which corresponds to the onset of melting the mixture of Bi_2O_3, Fe_3O_4 and $MnCO_3$ oxide powders. When the temperature is beyond 900ºC, a slight weight loss is observed on the TG curve, and an endothermic peak at 925ºC is also observed on the DSC curve, indicating the volatilization of the mixture of Bi_2O_3, Fe_3O_4 and $MnCO_3$ oxide powders, especially the Bi_2O_3 component. Therefore, in the system of mixed oxide powders of Bi_2O_3, Fe_3O_4 and $MnCO_3$, the sintering temperature should not be higher than 890ºC, otherwise, the ceramic samples will be melted together with the alumina crucible. Actually, in the experiment we find the ceramic samples sintered at 900ºC are melted and adhered to the walls of alumina crucible. Therefore, in this work, the sintering temperature of the BFMO ceramic samples is chosen as 880ºC.
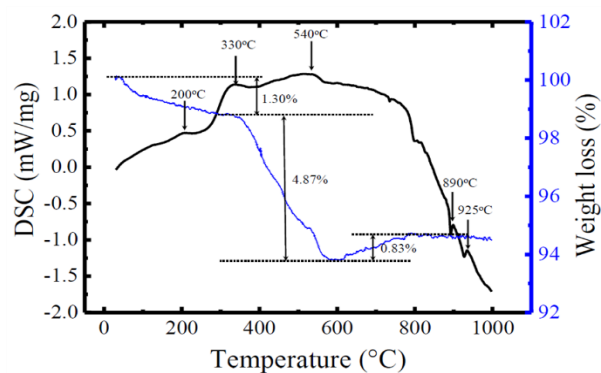

Fig. 1. DSC-TG curves of the mixed oxide powders of Bi_2O_3, Fe_3O_4 and $MnCO_3$.

Fig. 2 depicts the XRD pattern of the double-perovskite BFMO ceramics sintered at 880ºC for 3 h. It is found that there is a high structural similarity between BFO and the expected phase structure of BFMO, and therefore, BFO with R3c space group (JSCD no. 86-1518) is used to identify the perovskite phase of the BFMO ceramics. All the main diffraction peaks can be indexed by using a rhombohedral structure with space group R3c except the minor impure phase of Bi_2O_3 (JCPDS card No. 65-1209), indicating that the double-perovskite BFMO ceramics crystallize in a rhombohedral structure with R3c space group. The lattice parameters in the hexagonal crystal system for the BFMO ceramics were determined to be a = 5.571 Å and c = 13.191 Å. Therefore, the FeO_6 and MnO_6 polyhedrons are elongated along the [001] direction. Similar phenomenon was reported in the BFMO thin films [31]. The appearance of Bi_2O_3 impure phase is attributed to the excess Bi_2O_3 that is unreacted during the synthesized process.
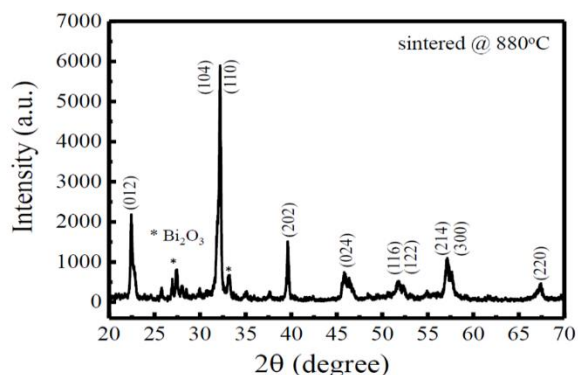
Fig. 2. XRD pattern of the double-perovskite BFMO ceramics synthesized by solid-state reaction and sintered at 880°C.
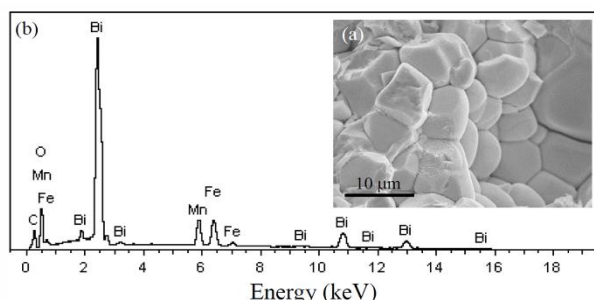

Fig. 3. (a) SEM image of the double-perovskite BFMO ceramics and (b) a representative EDS spectrum acquired from a BFMO ceramic grain.

Fig. 3(a) shows the SEM image of the double-perovskite BFMO ceramics, which reveals that the BFMO ceramic grains exhibit polyhedron morphology with an average size 6.70 μm. A representative EDS spectrum obtained from the BFMO ceramic grain in a mapping mode is displayed in **Fig. 3(b),** which confirms the presence of the constituent elements in the sample with an atomic ratio of 2.07:1.02:1 in the order of Bi, Fe, and Mn. That is very close to the stoichiometry of BFMO. The EDS data further confirm the successive synthesis of the BFMO ceramics.

Fig. 4 demonstrates the Raman spectrum of the BFMO ceramics measured room temperature. As it can be seen, the Raman spectrum is dominated by five strong Raman bands at around 123, 256, 292, 517, and 737 cm^{-1}, respectively. Other four weak Raman bands are also observed at around 141, 190, 580, and 820 cm^{-1}, respectively. The Raman modes can be identified as A_1-1 at 141 cm^{-1}, A_1-2 at 190 cm^{-1}, E (TO2) at 123 cm^{-1}, E (TO3) at 256 cm^{-1}, E (TO4) at 292 cm^{-1}, E (TO8) at 517 cm^{-1}, and E (TO9) at 580 cm^{-1}, respectively. The higher frequency Raman bands observed at 737 and 820 cm^{-1} can be attributed to the vibration of oxygen octahedral with Fe and Mn cations in their interiors. More precisely speaking, the strong Raman band observed at 737 cm^{-1} can be assigned to the A_g mode for the totally symmetric stretching of the MnO_6 octahedron, where the Bi atoms remain stationary and oxygen atoms move along the Fe-O-Mn axis. The weak Raman band near 820 cm^{-1} can be ascribed to the symmetrical stretching mode of $[(Fe/Mn)O_6]$ octahedron vibrational unit. In the double perovskite BFMO ceramics, Fe^{3+} and

Mn^{3+} ions occupy the B′ and B″ sites, respectively. The FeO_6 and MnO_6 octahedrons present a strong Jahn-Teller cooperative distortion, in conjunction with the octahedral tilting and the Fe/Mn cation disordering, lead to the structural lattice distortions. The relatively increased volume of the structurally distorted areas will result in a decrease in intensity of Raman band near 820 cm^{-1} [**38**]. To further analysis the Raman spectrum, the Lorentzian and Gaussian fits for the Raman spectrum of BFMO ceramics were performed, which are shown in **Fig. 4(a)** and **Fig. 4(b)**, respectively. The individual oscillators from the fits are also shown in **Fig. 4**. As shown in **Fig. 4(a)** fitted by Lorentzian oscillators, only 11 Raman bands at around 121, 145, 191, 258, 298, 342, 501, 522, 599, 737, and 823 cm^{-1}, are observed. Similarly, in **Fig. 4(b)** fitted by Gaussian oscillators, 11 Raman bands at around 120, 141, 193, 257, 295, 326, 497, 522, 589, 737, and 823 cm^{-1}, are observed. While the group theory predicts that in a single crystal with rhombohedral structure ($R3c$ space group) like BFMO, there exists 13 Raman active phonon modes represented by $\Gamma = 4A_1 + 9E$ at the center of the Brillouin zone [**39**]. However, in the present work only 11 Raman active modes are observed in the double-perovskite BFMO ceramics. The less Raman active modes observed in the double-perovskite BFMO ceramics can be ascribed to the small correlation field splitting of the ceramic samples due to their polycrystalline nature.
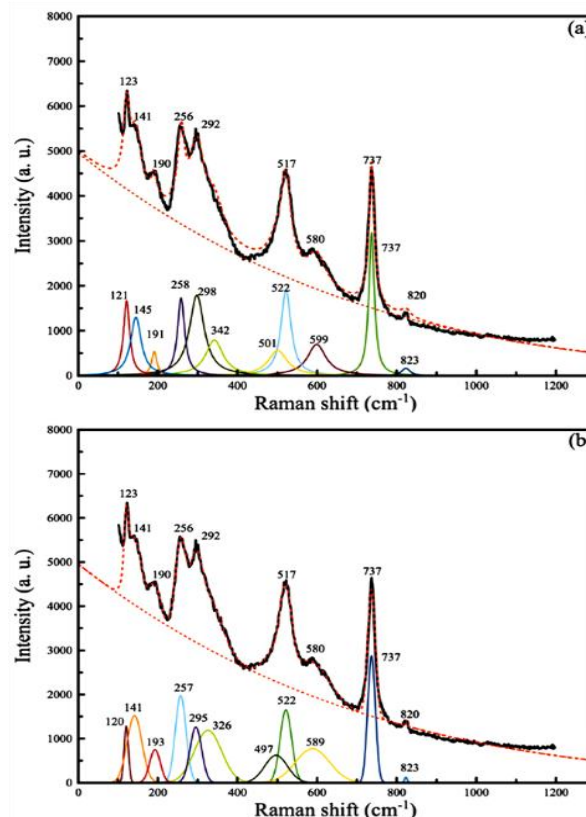

Fig. 4. Raman spectrum of the BFMO ceramics measured at room temperature. (a) Lorentzian and (b) Gaussian fits for the Raman spectrum, showing the individual oscillators from the fits. Black line is the observed data, red dashed line is the fitted spectrum, and the red dotted line is background of the Raman spectrum.
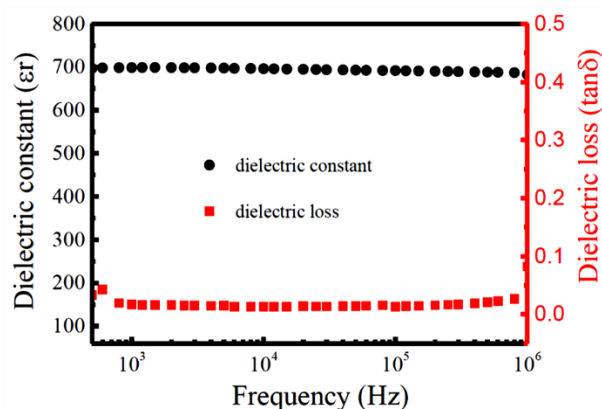
Fig. 5. Dielectric constants (ε_r) and dielectric losses ($\tan\delta$) of the BFMO ceramics measured as a function of the frequency.

Fig. 5 represents the frequency dependent dielectric properties of the BFMO ceramics. The dielectric constant of the BFMO ceramics exhibits almost frequency independent characteristics in the frequency range of $500 - 10^6$ Hz, which remains a constant value of 700. Such a value is much higher than that reported for the epitaxial BFMO thin films (the dielectric constant values for the BFMO(100), BFMO(110), and BFMO(111) thin films, are 130, 36, and 56 at 1 MHz, respectively) [32], and also much higher than that reported for the $BiFe_{0.70}Mn_{0.30}O_3$ magnetoelectric ceramics (the dielectric constant at 1 MHz is 65) [40] and the Mn-doped $Bi_{0.90}La_{0.10}Fe_{1-x}Mn_xO_3$ (x = 0.10, the dielectric constant at 1 MHz is 50) [41]. The corresponding dielectric loss for the BFMO ceramics also exhibits a similar frequency independent characteristics, which keeps a stable value of 0.03. The dielectric loss of the BFMO ceramics is much smaller than the values reported for the epitaxial BFMO thin films (e.g., the dielectric loss at 1 MHz for BFMO(100), BFMO(110), and BFMO(111) thin films, are 0.34, 0.20, and 0.38, respectively) [32], and for the $BiFe_{0.70}Mn_{0.30}O_3$ magnetoelectric ceramics (the dielectric loss at 1 MHz is 0.15) [40] and the Mn-doped $Bi_{0.90}La_{0.10}Fe_{1-x}Mn_xO_3$ (x = 0.10, the dielectric loss at 1 MHz is ~0.25) [41]. The present dielectric data of the double perovskite BFMO ceramics demonstrate that the BFMO ceramics exhibit almost frequency-independent dielectric behavior. Their high dielectric constant and low dielectric loss make the BFMO ceramics more attractive in the fields of nanoscale dielectric ceramic capacitors and resonators.

While the ferroelectricity in the double-perovskite BFMO thin film is confirmed by the local piezoelectric force microscopy hysteresis loop [33], however, the piezoelectric properties of double-perovskite oxides are rarely reported in the references. In this work, we perform piezoelectric measurements at room temperature. The piezoelectric modulus (d_{33}) of the BFMO ceramics was measured to be 56 pC/N, which is two times larger than that reported for the $BiFeO_3$ thin film ($d_{33} \cong 25$ pC/N) [42], and nearly 3 times of the value calculated for double-perovskite $CaMnTi_2O_6$

(d_{33} = 21.4 pC/N) [43], and nearly 6 times of the value for the epitaxial $BiFe_{0.9}Mn_{0.1}O_3$ thin films (d_{33} = 9.7 pC/N) [44]. Therefore, the BFMO ceramics display better piezoelectric response as compared with the $BiFeO_3$ ferroelectric perovskite oxide. Similar to many tetragonal ferroelectric perovskite oxides, BFMO can be also used as the end member compound to alloy with other ferroelectric oxides with rhombohedral symmetry. In this case, an enhanced piezoelectricity should be achieved around the morphotropic phase boundary in the BFMO-based solid solutions, like the case of $Pb(Zn_{1/3}Nb_{2/3})O_3$-$PbTiO_3$ solid solution [45].

Conclusion

In summary, polycrystalline double-perovskite BFMO oxide ceramics have been synthesized by solid-state reaction at 880°C. X-ray diffraction studies revealed that the BFMO ceramics crystallized in a rhombohedral structure with R3c space group. SEM image of the BFMO ceramics clearly shows the ceramic grains have a polyhedron morphology and contact closely with each other. The grain boundaries are much narrow and clean, and few voids are observed at the grain boundaries. The average grain size of the ceramic grains was measured to be 6.70 μm. Quantitative EDS data confirmed that the atomic ratio of Bi, Fe, and Mn elements in the BFMO ceramics was very close to the nominal value of 2.0:1.0:1.0. Eleven Raman active modes are observed in the Raman spectra of the BFMO ceramics, the fewer observed Raman modes as compared with those predicted by group theory can be attributed to the smaller correlation field splitting in the ceramic samples due to the polycrystalline nature. The BFMO ceramics exhibit almost frequency-independent dielectric behavior, and the dielectric constant and dielectric loss are 700 and 0.03 at 1MHz, respectively. The piezoelectric modulus (d_{33}) of the poled BFMO ceramics was measured to be 56 pC/N. The high dielectric constant and low dielectric loss make the BFMO ceramics to be promising candidate for dielectric ceramic capacitors and piezoelectric energy harvesters.

References

1. Catalan, G.; Scott, J. F.; *Adv. Mater.,* **2009**, 21, 2463.
2. Ma, J.; Hu, J.; Li, Z.; Nan, C. W.; *Adv. Mater.* **2011**, 23, 1062.
3. Li, J. F.; Wang, J. L.; Wuttig, M.; Ramesh, R.; Wang, N. G.; Ruette, B.; Pyatakov, A. P.; Zvezdin, A. K.; Viehland, D.; *Appl. Phys. Lett.* **2004**, 84, 5261.
4. Neaton, J. B.; Ederer, C.; Waghmare, U. V.; Spaldin, N. A.; Rabe, K. M.; *Phys. Rev. B,* **2005**, 71, 014113.
5. Ramesh, R.; Spaldin, N. A. *Nat. Mater.* **2007**, 6, 21.

6.　Sergienko, I. A.; Dagotto, E.; *Phys. Rev. B* **2006**, *73,* 094434.

7.　Heron, J. T.; Bosse, J. L.; He, Q.; Gao, Y.; Trassin, M.; Ye, L.; Clarkson, J. D.; Wang, C.; Liu, J. A.; Salahuddin, S.; Ralph, D. C.; Schlom, D. G.; Íñiguez, J.; Huey, B. D.; Ramesh, R.; *Nature* **2014**, *516,* 370.

8.　Bi, L.; Taussig, A. R.; Kim, H.; Wang, L.; Dionne, G. F.; Bono, D.; Persson, K.; Ceder, G.; Ross, C. A.; *Phys. Rev. B* **2008**, *78,* 104106.

9.　Ramesh, R.; Spaldin, N. A.; *Nature Mater.* **2007**, *6,* 21.

10.　Rogado, N. S.; Li, J.; Sleight, A. W.; Subramanian, M. A.; *Adv. Mater.* **2005**, *17,* 2225.

11.　Blasse, G.; *J. Phys. Chem. Solids* **1965**, *26,* 1969.

12.　Dass, R. I.; Yan, J. Q.; Goodenough, J. B.; *Phys. Rev. B,* **2003**, *68,* 064415.

13.　Dass, R. I.; Goodenough, J. B.; *Phys. Rev. B* **2003**, *67,* 014401.

14.　Azuma, M.; Takata, K.; Saito, T.; Ishiwata, S.; Shimakawa, Y.; Takano, M.; *J. Am. Chem. Soc.,* **2005**, *127,* 8889.

15.　Padhan, P.; Leclair, P.; Gupta, A.; Srinivasan, G.; *J. Phys.: Condens Matter,* **2008**, *20,* 355003.

16.　Du, Y.; Cheng, Z. X.; Wang, X. L.; Liu, P.; Dou, S. X.; *J. Appl. Phys.,* **2011**, *109,* 07B507.

17.　Ciucivara, A.; Sahu, B.; Kleinman, L.; *Phys. Rev. B,* **2007**, *76,* 3009.

18.　Ravi, S.; Senthilkumar, C.; *AIP Conf. Proc.,* **2015**, *1665,* 130007.

19.　Baettig, P.; Spaldin, N. A.; *Appl. Phys. Lett.,* **2005**, *86,* 012505.

20.　Nechache, R.; Harnagea, C.; Carignan, L. P.; Gautreau, O.; Pintilie, L.; Singh, M. P.; David, Ménard, D.; Fournier, P.; Alexe, M.; Pignolet, A.; *J. Appl. Phys.,* **2009**, *105,* 061621.

21.　Shimakawa, Y.; Azuma, M.; Ichikawa, N.; *Materials,* **2011**, *4,* 153.

22.　Pei, Z. P.; Lu, Y.; Wu, H.; Xia, W. R.; Zhu, X. H.; *J. Chin. Cram. Soc.,* **2019**, *47,* 518.

23.　Zhao, H. Y.; Kimura, H.; Cheng, Z. X.; Wang, X. L.; Ozawa, K.; Nishida, T.; *J. Appl. Phys.,* **2010**, *108,* 093903.

24.　Zhao, H. Y.; Kimura, H.; Yao, Q.W.; Du, Y.; Cheng, Z. X.; Wang, X. L.; New multiferroic materials: Bi_2FeMnO_6, In Ferroelectrics-Materials Aspects; Larrart, M. (Eds.); InTech: Croatia, Europe, **2011**, pp. 237-250.

25.　Delmonte, D.; Mezzadri, F.; Gilioli, E.; Solzi, M.; Calestani, G.; Bolzoni, F.; Cabassi, R.; *Inorg. Chem.,* **2016**, *55,* 6308.

26.　Gilioli, E.; Ehm, L.; *IUCRj,* **2014**, *1,* 590.

27.　Zhao, H. Y.; Kimura, H.; Cheng, Z. X.; Wang, X. L.; Nishida, T.; *Appl. Phys. Lett.,* **2009**, *95,* 232904.

28.　Choi, E. M.; Patnaik, S.; Weal, E.; Sahonta, S. L.; Wang, H.; Bi, Z.; Xiong, J.; Blamire, M. G.; Jia, Q. X.; MacManus-Driscoll, J. L.; *Appl. Phys. Lett.,* **2011**, *98,* 012509.

29.　Ahmed, T.; Chen, A.; McFarland, B.; Wang, Q.; Ohldag, H.; Sandberg, R.; Jia, Q.; Yarotski, D. A.; Zhu, J. X.; *Appl. Phys. Lett.,* **2016**, *108,* 242907.

30.　Ahmed, T.; Chen, A.; Yarotski, D. A.; Trugman, S. A.; Jia, Q.; Zhu, J. X.; *APL Mater.* **2017**, *5,* 035601.

31.　Du, Y.; Cheng, Z. X.; Dou, S. X.; Wang, X. L.; Zhao, H. Y.; Kimura, H.; *Appl. Phys. Lett.,* **2010**, *97,* 122502.

32.　Liu, P.; Cheng, Z. X.; Du, Y.; Feng, L. Y.; Fang, H.; Wang, X. L.; Dou, S. X.; *J. Appl. Phys.,* **2013**, *113,* 17D904.

33.　Sun, L.; Fang, Y. W.; He, J.; Zhang, Y. Y.; Qi, R. J.; He, Q.; Huang, R.; Xiang, P. H.; Tang, X. D.; Yang, P. X.; Chu, J. H.; Chu, Y. H.; Duan, C. G.; *J. Mater. Chem. C,* **2017**, *5,* 5494.

34.　Shen, P.; Guan Z.; Zhong N.; Xiang P. H.; Wang, R. B.; Bao, Q. Y.; Yang, P. X.; Sun, L.; Duan, C. G.; Chu, J. H.; *J. Phys. D: Appl. Phys.,* **2018**, *51,* 045304.

35.　Ghosh, A.; Ahmed, T.; Yarotski, D. A.; Nakhmanson, S. M.; Zhu, J. X.; *EPL,* **2016**, *116,* 57002.

36.　Du, Y.; Cheng, Z. X.; Zhao, H. Y.; Kimura, H.; Zhang, P.; Guo, Z. P.; Wang, X. L.; *Curr. Appl. Phys.,* **2011**, *11,* S236.

37.　Xu, N. C.; Liu, Z.; Bian, S. J.; Dong, Y. P.; Li, W.; *Mater. Rev.* **2016**, *30,* 39.

38.　Iliev, M. N.; Abrashev, M. N.; Popov,V. N.; Hadjiev, V. G.; *Phys. Rev. B,* **2003**, *67,* 212301.

39.　Kamba, S.; Nuzhnyy, D.; Savinov, M.; Šebek, J.; Petzelt, J.; Prokleška, J.; Haumont, R.; Kreisel, J.; *Phys. Rev. B,* **2007**, *75,* 024403.

40.　Ianculescu, A.; Gheorghiu, F. P.; Postolache, P.; Oprea, O.; Mitoseriu, L. T.; *J. Alloys Compd.,* **2010**, *504,* 420.

41.　Pradhan, D. K.; Choudhary, R. N. P.; Rinaldi, C.; Katiyar, R. S.; *J. Appl. Phys.,* **2009**, *106,* 024102.

42.　Daumont, C.; Ren, W.; Infante, I. C.; Lisenkov, S.; Allibe, J.; Carrétéro, C.; Fusil, S.; Jacquet, E.; Bouvet, T.; Bouamrane, F.; Prosandeev, S.; Geneste, G.; Dkhil, B.; Bellaiche, L.; Barthélémy, A.; Bibes, M.; *J. Phys.: Condens. Matter.,* **2012**, *24,* 162202.

43.　Gou, G. Y.; Charles, N.; Shi, J.; Rondinelli, J. M.; *Inorg. Chem.* **2017**, *56,* 11854.

44.　Lee, S. H.; Yang, C.H.; Jeong, Y. H.; Birge, N. O.; *Phys. B: Condens. Matter.,* **2006**, *383,* 31.

45.　Noheda, B.; Cox, D. E.; Shirane, G.; Park, S. E.; Cross, L. E.; Zhong, Z.; *Phys. Rev. Lett.,* **2001**, *86,* 3891.